Review

Nanostructured Iridium Oxide: State of the Art

Francesca Scarpelli [1], Nicolas Godbert [1,2,*] , Alessandra Crispini [1,2] and Iolinda Aiello [1,2,3]

1   MAT-InLAB (Laboratorio di Materiali Molecolari Inorganici), LASCAMM-CR INSTM, Unità INSTM della Calabria, Dipartimento di Chimica e Tecnologie Chimiche, Università della Calabria, 87036 Rende, CS, Italy
2   LPM-Laboratorio Preparazione Materiali, Star-Lab, Via Tito Flavio, 87036 Rende, CS, Italy
3   CNR NANOTEC, Institute of Nanotechnology, U.O.S. Cosenza, 87036 Rende, CS, Italy
*   Correspondence: nicolas.godbert@unical.it

Abstract: Iridium Oxide (IrO_2) is a metal oxide with a rutile crystalline structure, analogous to the TiO_2 rutile polymorph. Unlike other oxides of transition metals, IrO_2 shows a metallic type conductivity and displays a low surface work function. IrO_2 is also characterized by a high chemical stability. These highly desirable properties make IrO_2 a rightful candidate for specific applications. Furthermore, IrO_2 can be synthesized in the form of a wide variety of nanostructures ranging from nanopowder, nanosheets, nanotubes, nanorods, nanowires, and nanoporous thin films. IrO_2 nanostructuration, which allows its attractive intrinsic properties to be enhanced, can therefore be exploited according to the pursued application. Indeed, IrO_2 nanostructures have shown utility in fields that span from electrocatalysis, electrochromic devices, sensors, fuel cell and supercapacitors. After a brief description of the IrO_2 structure and properties, the present review will describe the main employed synthetic methodologies that are followed to prepare selectively the various types of nanostructures, highlighting in each case the advantages brought by the nanostructuration illustrating their performances and applications.

Keywords: iridium oxide; nanostructuration; IrO_2 applications; IrO_2 synthesis; OER

1. Introduction

Iridium Oxide (IrO_2) is a noble metal oxide with a rutile crystalline structure [1], with a $P4_2/mnm$ space group. The rutile structure is characterized by a tetragonal unit cell in which every Iridium ion is coordinated to six Oxygen ions, adopting an octahedral geometry (Figure 1).
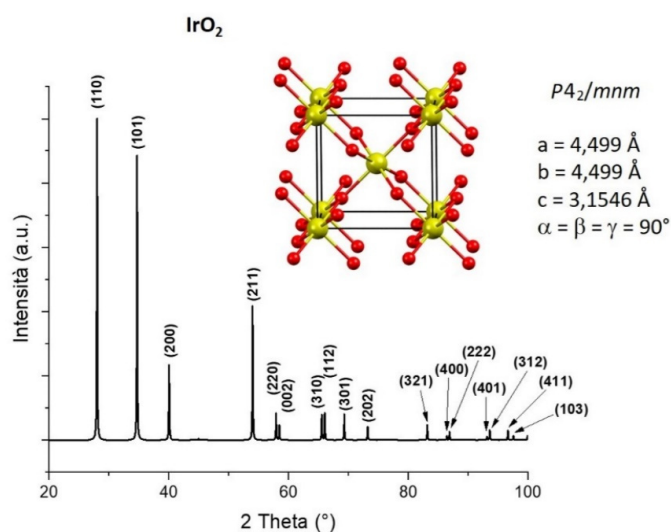
Figure 1. Unit cell, cell parameters and X-ray diffraction pattern with relative (hkl) indexation of IrO_2, information extracted from deposited crystal structure (yellow: Ir atoms, red: O atoms) [2].

Unlike other transition metal oxides, IrO_2 shows a metallic-type conductivity ($\sim10^4$ S·cm^{-1}) [3]. The reason for this behaviour was first investigated by Gillson et al. [1]: IrO_2, like other dioxides with a rutile-related structure, have incompletely filled *d* shells [IrO_2 (5d^5)]. Later, Verbist et al. [4], used X-ray Photoelectron Spectroscopy, to confirm the presence of a partially filled electron band in IrO_2, having a *d* character, just at the Fermi level, which could be responsible of the high conductivity of the metal oxide. Besides its high electrical conductivity, IrO_2 is also characterized by high chemical stability, low surface work function (4.23 eV) [5] and good stability under the influence of a high electric fields. Note that the work function (energy required for moving an electron from the Fermi level to the local vacuum level) is a surface sensitive property and typically depends on the electron chemical potential and the polarisation of the surface. Consequently, the work function can be modulated by several factors in particular the surface roughness and the orientation of the crystal lattice (i.e., which crystal face is mostly exposed). However, the more significant parameter to tune the work function of metal oxides would probably be the superficial oxygen vacancies [6]. Consequently, nanostructuration of metal oxides will have a great influence on the overall work function of the produced material. Table 1 reports the average work function of the most frequently studied metal oxides in comparison to IrO_2, considering thin films of polycrystalline metal oxide (i.e., without any preferred surface direction growth).

Table 1. Work functions and conductive characteristics of some metal-oxides.

Metal Oxide	Work Function (eV) *	Conductivity
IrO_2	4.23 [5]	Metallic (ca. 10^4 S·cm^{-1}) [7]
TiO	4.7 [8]	Metallic (5882 S·cm^{-1}) [9]
ReO_3	6.75 [10]	Metallic (ca.10^5 S·cm^{-1}) [11]
MoO_2	5.9 [8]	Metallic (3355S·cm^{-1}) [12]
RuO_2	5.2 [13]	Metallic (ca. $1,3.10^4$ S·cm^{-1}) [14]
NiO	6.3 [8]	*p*-type semiconductor, band gap 4 eV [15]
CuO	5.9 [8]	*p*-type semiconductor, band gap 1.5 eV [16]
Cu_2O	4.9 [8]	*p*-type semiconductor, band gap 2.40 eV [17]
Co_3O_4	6.3 [8]	*p*-type semiconductor, band gap 2.07eV [18]
CoO	4.6 [8]	*p*-type semiconductor, band gap 2.6eV [19]
Rh_2O_3	*n.r.* **	*p*-type semiconductor, band gap 1.4 eV for Rh_2O_3(I) and 1.2 for Rh_2O_3(III) [14]
TiO_2	5.4 [8]	*n*-type semiconductor, band gap anatase 3.2eV, rutile 3.0 eV [20]
MoO_3	6.82 [8]	*n*-type semiconductor, α-MoO_3band gap 3.2 eV [21]
WO_3	6.8 [8]	*n*-type semiconductor, band gap 2.75 eV [22]
SnO_2	4.75 [23]	*n*-type semiconductor, band gap 3.6 eV [24]
In_2O_3	5.0 [25]	*n*-type semiconductor, band gap 3.75 eV [26]
ZnO	4.71 [27]	*n*-type semiconductor, 3.3 eV [28]
ZrO_2	3.1 [29]	insulator
V_2O_5	7.0 [30]	insulator-metal transition (275 °C) [6]
V_2O_3	4.9 [8]	insulator-metal transition (−111 °C) [31]

* reported on polycrystalline thin film. ** not reported (to the best of our knowledge).

The appealing properties displayed by IrO_2 enable its use in many applications despite its relatively high cost. The main application fields of IrO_2 are summarized in Table 2 together with their challenging issues that are still nowadays to overcome.

In particular, IrO_2 plays a pivotal role in water electrolysis, the process in which water is split into hydrogen and oxygen gases, by means of the passing of an electric current. This process, if driven by renewable energy (solar or wind), can produce high-quality and clean hydrogen, as an energy source alternative to fossil fuels. Specifically, IrO_2 is considered one of the most active electrocatalysts for Oxygen Evolution Reaction (OER), the anodic reaction of water electrolysis, in which water is oxidized to molecular oxygen. OER represents the limiting process in water electrolysis, which determines the cell

voltage and therefore the energy consumption of the process [32]. IrO_2 have been shown to possess very high electrocatalytic activity for OER, improving the process efficiency [33,34]. Several computational studies, electrochemical studies and characterization techniques, including, X-ray absorption near-edge structure, near-edge X-ray absorption fine structure, X-ray absorption, X-ray photoelectron, and Raman spectroscopies, have been devoted to understanding the OER mechanism over IrO_2 [35–37]. According to Nilsson et al. [37], IrO_2 surface in contact with water undergoes to a partial hydroxylation, showing hydroxide sites which coexist with the oxide sites. During OER, the hydroxide sites are converted into oxide sites, passing through an -OOH as intermediate. The simultaneous formation of some Ir(V) centres was ascertained, which could be responsible for the catalytic activity of IrO_2 toward OER, since its subsequent two-electrons reduction to Ir(III) can be sufficient to oxidize water in an oxygen molecule. However, several possible OER catalytic cycles over IrO_2, recently reviewed by Naito et al., have been proposed [35]. Specifically, the catalytic cycle can proceed via the oxidation-reduction reactions of either the Iridium centre or the absorbed O species or the Ir=O states. A catalytic cycle driven by the releasing and filling of an oxygen vacancy at the IrO_2 surface has also been suggested. Full understanding of the OER mechanism over Iridium is thus a contemporary and challenging issue that still requires attention for the design of future efficient IrO_2 based catalysts.

Moreover, IrO_2 is an electrochromic (EC) material that displays a reversible and persistent colour change under an external electric field, thus finding application in electrochromic devices. The change in its optical properties may be ascribed to the following reaction [38], as shown in Scheme 1:

$$\text{Ir (OH)}_3 \rightleftharpoons \text{IrO}_2\cdot\text{H}_2\text{O} + \text{H}^+ + \text{e}^-$$

transparent   blue-black
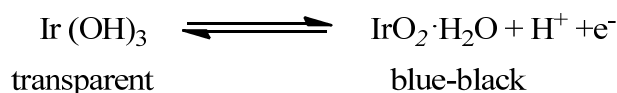
Scheme 1. Redox reaction at the basis of IrO2 EC properties.

During colouring, electrons and protons are removed from the material by application of an anodic potential, whereas during bleaching electrons and protons are injected into the substrate [39]. In its lower oxidation states [Ir(III)], Iridium (hydr)oxide is transparent, while in its higher oxidation state [Ir(IV)], IrO_2 turns to a blue-black colour due to a strong absorption in the visible spectral region [40]. IrO_2 presents several ideal features for an EC material, such as fast colour change, good open-circuit memory, and long last durability (more than 10^7 cycle lives) [40,41], which promote its application in EC devices [41–44].

Notably, the transition between two oxidation states [Ir(III) and Ir(IV)] is also exploited for the fabrication of IrO_2 based pH sensors [45–48]. Owing to proton–electron double injection, IrO_2 is reduced to Ir(OH)$_3$ during pH detection [47]. IrO_2 provides a fast-potentiometric response to pH change, thanks to its high conductivity. IrO_2-based electrodes have useful properties, such as high stability in a wide range of temperature (from $-20\,°C$ to $250\,°C$) [49–51], linear response in a broad pH range (from pH = 0 to pH = 12) [50,52,53], great chemical stability, and low impedance [54]. Moreover, IrO_2-based electrodes could be used in many application fields, since their pH response is not affected by most anions present in environmental systems, such as Na^+, K^+, Li^+, Mg^{2+}, Ca^{2+}, Cl^-, Br^-, NO_3^-, nor by the main complexing agents present in biological systems, such as citrate, lactate and phosphate [53]. For these reasons, IrO_2 has been widely employed for the sensing of glucose, hydrogen peroxide, glutamate, metal ions, organophosphates, and pesticides [55]. Furthermore, the Food and Drug Administration approved IrO_2 as a high biocompatible material, facilitating its application in biosensors [56,57], probe for fluorescence imaging [58], photodynamic/photothermal therapy [59], and stimulating and recording electrodes [60,61]. To this end, due to its high charge capacity, for a given applied voltage pulse, IrO_2 is able to inject a very high charge density [62].

By virtue of its conductive nature, high chemical stability, low surface work function (4.23 eV) and stability under influence of high electric fields, IrO_2 has been used as field emitter cathode in vacuum microelectronics [63–65]. Indeed, IrO_2 doesn't suffer from

the eventual presence of residual Oxygen in these devices, contrary to other metals, as Molybdenum, that reacts quickly with O_2 forming an insulating layer of oxide [66].

Further applications of IrO_2 include electrode material for direct methanol fuel cell (DMFC) [67], for supercapacitors [68], and for neural stimulation [69]. Specifically, the anodic reaction in a DMFC, in which methanol is oxidized to carbon dioxide, can be efficiently catalysed by IrO_2 [67]. Moreover, IrO_2, thanks to its ability to store electricity, can be an excellent negative electrode for electrochemical capacitors [68].

Table 2. Main applications of IrO_2-based materials.

Application	Main Features	Refs.	Current Challenge
Electrochromic devices	Fast colour change	[40,42,70]	Application in flexible devices (IrO_2 is a rigid material)
OER	High catalytic activity High stability in acidic media	[71–75]	Deep understanding of the OER mechanism over IrO_2
Sensing	Stability repeatability	[46,47,55] [76,77]	Standardization of electrode preparation methods (dependence of pH response of IrO_2) Improvement of stability over the pH range of 12–14 Improve sensing sensitivity Lowering the working temperature in gas sensing
Supercapacitor	High conductivity	[68,78]	Increase of the durability of the electrode (slight worsening of performance after 2000 charge/discharge cycles at 0.5 mA)
Field Emission Cathode	Low chemical reactivity Thermal stability Low work function	[65,79,80]	Achieve high aspect structures to enable operation at low applied fields Insure long-term device operation under adverse vacuum conditions

Noticeably, the above-described applications of IrO_2 can benefit from the use of nanostructures instead of bulk IrO_2. Indeed, all the intrinsic properties of IrO_2, as well as for other transition metal oxides, can be improved through its nanostructuration. Thus, the synthesis of IrO_2 in its nanostructured form (structures presenting at least one dimension on the nanoscale) has become an increasing field of interest in research. In particular, nanostructured materials that exhibit chemical, optical, mechanical and electrical properties modified with respect to the corresponding bulk material, due to size and quantum effects [81–86]. Several types of nanostructures, with different dimensionality, are known, including zero-dimensional (0D, quantum dots and nanopowder), one-dimensional (1D, nanotubes, nanowires and nanorods), and two-dimensional (2D, nanostructured films)

nanomaterials [86]. Whatever the dimensionality of the nanomaterials, it is preferable that the nanostructures are well separated from each other, as an over-aggregation could determine the loss of the nanostructuration with the appearance of properties that are more reminiscent of those of a bulk material.

To this regard, IrO_2 can be synthesized in the form of various types of nanostructures, as nanoparticles with undefined shape, i.e., nanopowders, [87] and nanoparticles with a precise shape, including nanosheets [88], nanorods [5,89], nanotubes [76], nanowires [48,90], and nanoporous films [91,92]. Herein, we provide an overview on the nanostructuration of IrO_2, with special emphasis on the strategies pursued for the synthesis of IrO_2 nanostructures. Indeed, up to now many preparation procedures of IrO_2 nanostructures have been described in the literature, including soft- and hard-template routes, hydrothermal synthesis, colloidal methods, and many others. It is worth noting that, within the same preparation method, by finely tuning the experimental parameters, nanostructures with different shapes can also be synthetized. On this basis, we focused our attention on the shapes and morphologies that can be obtained through the different preparation methodologies, since the shape/morphology determine the physical and chemical properties of IrO_2 nanostructures. Furthermore, when available, the performances of these IrO_2 nanostructures in specific applications will be described.

2. IrO_2 Spherical Nanoparticles and Nanopowder

The synthesis methods, characterization and description of specific applications of IrO_2 spherical nanoparticles have been brilliantly reported recently by J. Quinson [93]. Interested readers are directed towards his report for a deeper overview, especially for what concerns the analysis about the difficulty to fully distinguish between Ir and IrO_x nanoparticles during their preparation [93]. Thus, in the following part of this review, we will only focus on the main synthesis pathways used to prepare IrO_2 as nanopowder. Several methods to synthesize IrO_2 nanopowder, meaning nanoparticles with undefined shape, have been experimented. In 2005, Marshall introduced a modification to the well-known polyol method, usually used for the preparation of metallic nanoparticles [94,95]. This procedure consists in dissolving or dispersing the metallic precursor, usually hexachloroiridic acid ($H_2IrCl_6 \cdot nH_2O$), in a polyol, such as ethylene glycol, which acts both as solvent and as reducing agent. Upon refluxing the reaction mixture, a metallic precipitate, composed of Ir nanoparticles with an average size of about 3 nm, is formed, which is then filtered and dried. The colloid is finally calcinated to ensure the full oxidation of the obtained product.

Another approach is represented by the Adams fusion method [96], in which the metallic precursor H_2IrCl_6 is melted together with $NaNO_3$. The possible reactions that may occur during the process are shown in Scheme 2. Basically, when H_2IrCl_6 is melted together with $NaNO_3$, $Ir(NO_3)_4$ is formed. This latter, at high temperature (ca. 460 °C) decomposes, thus generating IrO_2.

$$H_2IrCl_6 + 6NaNO_3 \longrightarrow 6NaCl + Ir(NO_3)_4 + 2HNO_3$$

$$Ir(NO_3)_4 \longrightarrow IrO_2 + 4NO_2 + O_2$$
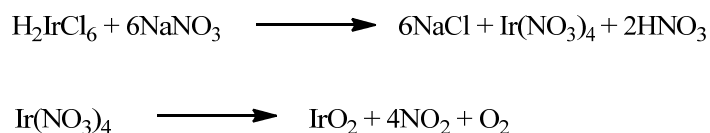
Scheme 2. The hypothesized reactions taking place in the Adams fusion method [94].

After cooling, the mixture is thoroughly washed with water to remove salt residues, nitrites, and nitrates. Despite the simplicity of this method, a long purification step is required, and sodium traces may remain in the metal oxide powder.

Nanosized IrO_2 powder can also be synthesized through the colloidal method [97,98]. This process involves the addition of NaOH to a water solution of the Iridium precursor, $H_2IrCl_6 \cdot nH_2O$, to induce the formation of an Ir-hydroxide. The resulting colloidal solution is heated at 80–100 °C, then washed, dried, and calcinated at 400 °C to obtain colloidal IrO_2, composed of IrO_2 nanoparticles with an average size of diameter ca. 7 nm. However,

although the simplicity of the method and the fact that no specific experimental set up is required, the final product remains of a colloid state, thus the nanoparticles are all aggregated to each other as shown in the reported Transmission Electron Microscopy (TEM) micrograph (Figure 2). Nevertheless, the as-synthesized nanopowder was tested as electrocatalyst for OER in a solid polymer electrolyte electrolyzer, demonstrating high stability and higher activity with respect to commercial IrO_2 powder, which does not feature any nanostructuration [97].
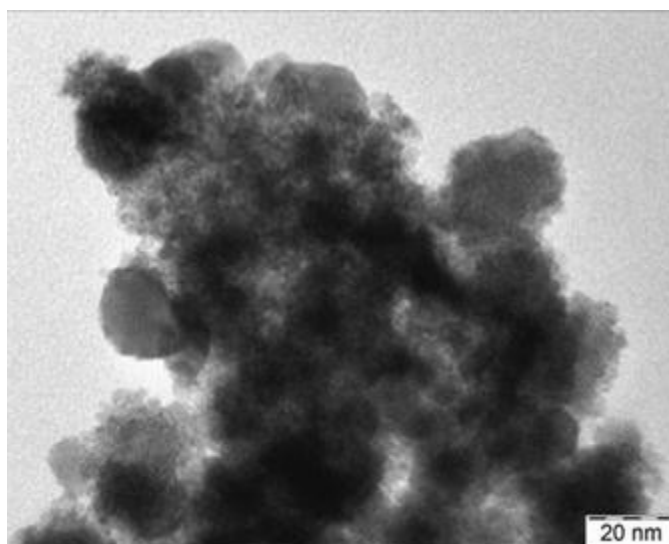
Figure 2. TEM micrograph of colloidal IrO_2 obtained through the colloidal method (Reprinted/adapted with permission from Ref. [97]).

The colloidal method, which involves an initial alkaline hydrolysis of the Iridium precursor (K_2IrCl_6) in water solution at high temperature, can also be carried out without the calcinations step, thus further simplifying the method, as reported by Khalil et al. [77]. By applying this procedure, IrO_2 nanoparticles with an average size of 1–2 nm have been obtained (Figure 3). However, also in this case, the particles are aggregated with each other, due to the absence of a capping agent. The same authors described the preparation of a pH electrode through the electrodeposition of the as-prepared IrO_2 nanopowder on an Au substrate and the evaluation of its potentiometric responses in pH buffer solutions between pH 1.68 to 12.36. The electrode demonstrated excellent pH sensitivity (−73.7 mV/pH unit), with a super-Nernstian response [77].
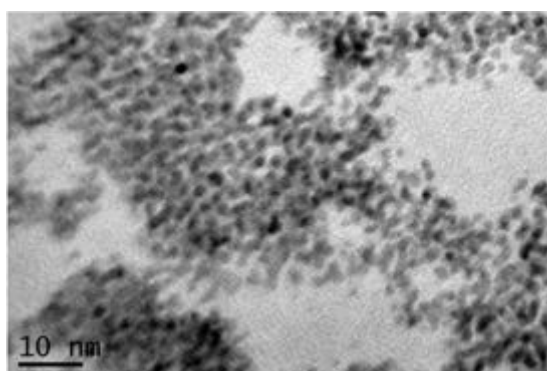
Figure 3. TEM image of colloidal iridium nanoparticles (Reprinted/adapted with permission from Ref. [77]).

Recently, the synthesis of colloidal IrO_2 has been also performed through a microwave-assisted route which combines the colloidal and polyol methods, and avoids the calcinations step [87]. Ethylene glycol was used as solvent, whereas NaOH was used as source of OH^- anions, to generate the Ir-hydroxide intermediate. The reaction was carried out under microwave irradiation, until the colour solution turned to dark brown, indicating the formation of IrO_2 colloidal suspensions. Specifically, the metal oxide was formed when the solution reached its boiling point, without requiring a high temperature treatment in a muffle furnace. The obtained colloidal suspension was stable against flocculation and exhibited a low polydispersity. Moreover, the same method can be carried out in milder reaction conditions, by using alcohols with a low boiling point, such as methanol or ethanol, instead of ethylene glycol.

Finally, nanosized IrO_2 powder can be effectively synthesized through the soft-template route, by using an organic polymer as templating agent [99,100]. Specifically, Zhang et al. described a process in which nanostructuration of Iridium Oxide is achieved by the in-situ polymerization of pyrrole in a water solution containing the Iridium precursor $(NH_4)_2IrCl_6$, followed by thermal annealing of the nanocomposite (Figure 4) [99]. At a temperature value of 450 °C, the organic part of the composite is totally degraded, and Iridium Oxide nanoparticles, can be recovered. The high surface area displayed by these materials corresponds to a great number of accessible electrochemical sites. Indeed, the as-prepared nanosized Iridium Oxide exhibits a greater electrocatalytic efficiency towards OER, when compared to commercial IrO_2 [99]. In particular, the nanostructured iridium oxide exhibits low overpotential (291.3 ± 6 mV) to reach 10 mA/cm^2 current density towards OER and higher stability with respect to commercial IrO_2.
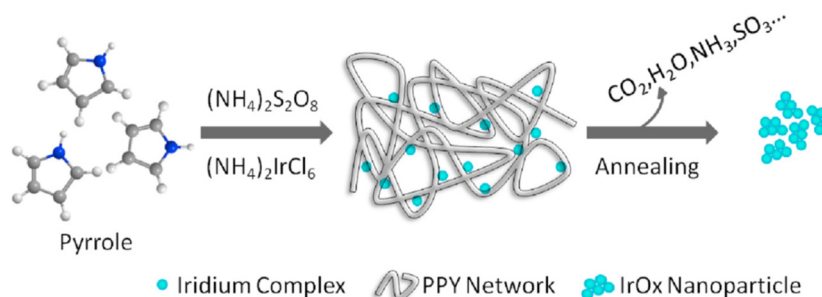
Figure 4. A schematic representation of the soft-template route for the synthesis of Iridium Oxide nanoparticles (Reprinted/adapted with permission from Ref. [99]).

3. IrO$_2$ 1D-Nanostructures

1D nanostructures present only one dimension greater than 100 nm, while the others are a few nanometers long. These nanostructures include nanotubes, nanorods and nanowires, and they usually display greater resistance to agglomeration with respect to nanopowder. These elongated structures, as well as nanopowder, exhibit superior properties with respect to bulk materials [86]. Moreover, theoretical studies recently have highlighted the superior electrocatalytic performances of IrO_2 1D-nanostructures, specifically IrO_2 nanowires, with respect to IrO_2 nanospheres, thanks to their regular and periodic structure, without the tendency to agglomeration [71]. In the following part of the review, the IrO_2 1D-nanostructures and the main methodologies for their synthesis will be described according to their specific shape.

3.1. IrO$_2$ Nanotubes

IrO_2 nanotubes have been built using a hard-templating route coupled with electrodeposition (Figure 5). Concretely, an anodic aluminium oxide (AAO) layer with large pores was first fabricated through the sputtering of an aluminium layer on a silicon substrate, followed by an anodization process. IrO_2 was electrodeposited on this template layer,

generating nanotubes which grew along the walls of the AAO nanopores. At the end of the process, the AAO template was removed by dissolution in concentrated KOH solution [76].

As reported by Chiao et al., the shape and the length of the nanotubes prepared through this method depend on the morphology of the nanoporous AAO template, whereas the wall thickness of the nanotubes is finely controlled by the electrodeposition time [76]. The nanotubes obtained by Chiao et al., analysed by Scanning Electron Microscopy (SEM), show a diameter of 50 nm and length of around 750 nm. However, the not uncommon presence of defective nanopores in the AAO template, results in the formation of incomplete and collapsed nanotubes together with hollow nanotubes.
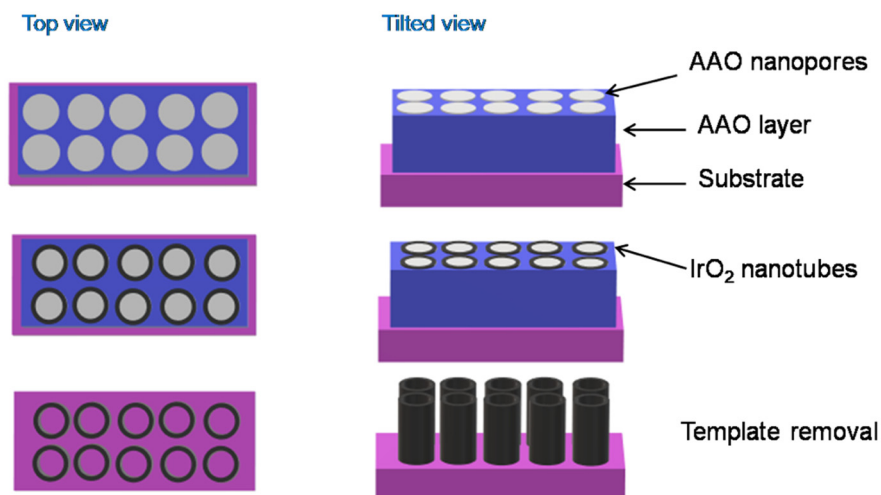
Figure 5. A schematic representation of the hard-template route for the synthesis of IrO_2 nanotubes.

A more uniformly distributed IrO_2 nanotubes array has been obtained by using the hard template route coupled to an acidic chemical bath, instead of electrodeposition, allowing to produce IrO_2 nanotubes [101]. Specifically, the AAO template has been soaked in a solution containing the Iridium precursor, Na_3IrCl_6, in addition to NaClO, HNO_3 and H_2O_2, generating, in 24 h and after acidic removal of the AAO template, a uniform film, with a thickness of 60 nm and a length of 400 nm, composed of IrO_2 nanotubes (Figure 6). The as-prepared nanotubes array exhibited a large charge storage capacity, measured through electrochemical analysis, proving its potential application as neural-electronic interface electrode [101].
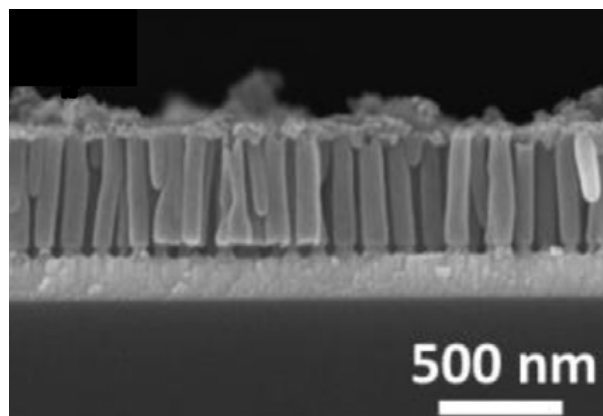
Figure 6. SEM image of IrO_2 nanotubes array (Reprinted/adapted with permission from Ref. [101]).

Recently, IrO_2 nanotubes have been synthesized without a hard template, by electro-spinning and calcination techniques [102]. Specifically, a solution containing the Iridium

precursor $IrCl_3$ was electrospun on an aluminium plate, then calcinated at 500 °C, under O_2 and He flow, recovering IrO_2 nanotubes after cooling. However, although the authors claim to prepare IrO_2 nanotubes without any template, the initial solution also contains poly(vinylpyrrolidone) (PVP), which, as stated by the authors, acts as a "framework", and is removed through the thermal annealing. The as-synthetized IrO_2 nanotubes were tested as electrode material for amperometric CO sensing, but they resulted in poorly electroactive towards electrochemical CO oxidation, in contrast to the metallic counterparts, i.e., Ir nanotubes that were produced by the reduction, under H_2 and Ar flow, of the as-prepared IrO_2 nanotubes.

Finally, IrO_2 nanotubes can be efficiently prepared through Metal-Organic Chemical Vapor Deposition (MOCVD) [103]. This method, however, requires a specifically designed reactor in which ultra-pure gases are injected to transport and react with the organometallic precursor. By applying this methodology, IrO_2 nanotubes have been successfully grown on a $LiTaO_3$ substrate using a low-melting Iridium source, (Methylcyclopentadienyl) (1,5-cyclooctadiene) Iridium(I), [(MeCp)Ir(COD)] (chemical structure reported in Figure 7), a high oxygen pressure (20–50 Torr), and a temperature of ca. 350 °C [103]. The as-obtained nanostructures, presenting an unusual square cross-section, present a tilt angle of 35° ca. with respect to the normal to the substrate surface and are perfectly aligned with each other (Figure 7a).
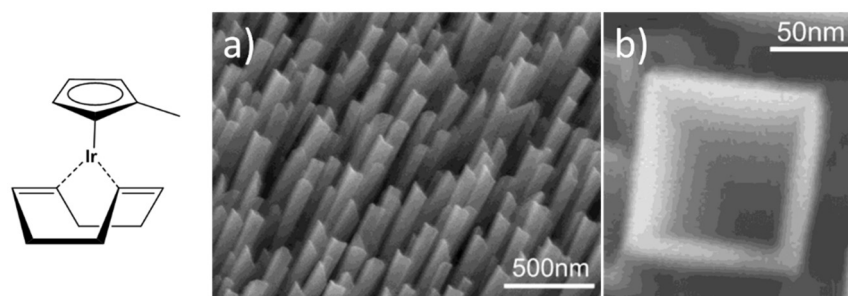
Figure 7. Chemical structure of [(MeCp)Ir(COD)] and SEM micrographs at different magnifications of IrO_2 nanotubes synthetized through MOCVD, (**a**) top view of IrO_2 nanotubes, (**b**) a wedge-shaped rod (Reprinted/adapted with permission from Ref. [103]).

Notably, by opportunely modifying the experimental parameters used during the MOCVD, the same authors were able to finely tune the shape of the obtained nanotubes, thus obtaining forms ranging from nearly-triangular nanorods, wedge-like nanorods (Figure 7b) and scrolled nanotubes of IrO_2. Indeed, the growth of these peculiar structures, and in particular their shape, is highly dependent on the substrate temperature and the degree of supersaturation, this latter being controlled by the temperature of the precursor reservoir [104]. Interestingly, these square hollowed IrO_2 nanotubes grown onto sapphire (100) substrate were successfully reduced to mixed $Ir-IrO_2$ nanotubes by high vacuum thermal annealing. Moreover, a Pt electrodeposition was carried-out on these nanotubes to generate a new nanostructured catalyst for methanol oxidation, with activity comparable to that of a commercial PtRu catalyst [105].

3.2. IrO₂ Nanorods

IrO_2 nanorods can be produced through several techniques, including the hard-template route [89], the "molten salt" method [106], and MOCVD [5]. In particular, similarly to IrO_2 nanotubes [76,101], arrays of IrO_2 nanorods have been synthetized using AAO membranes as hard template [89]. In these cases, the porous AAO membrane has been soaked in an alkaline chemical bath, containing $IrCl_4$, as Iridium precursor, and K_2CO_3 as source of OH^- anions. The temperature was increased to 95 °C, allowing the reactions reported in Scheme 3 to take place. Basically, the OH^- anions which derived from the

reaction of K_2CO_3 with water, react with the Iridium precursor generating the Ir-hydroxyde intermediate which evolves towards the formation of IrO_2.

$$K_2CO_3 + H_2O \longrightarrow 2K^+ + 2OH^- + CO_2$$

$$IrCl_4 + OH^- \longrightarrow IrO_2 + H_2O + Cl^-$$
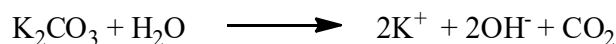
Scheme 3. The reactions taking place in the chemical bath method to synthetize IrO_2 nanorods on AAO membranes [89].

The IrO_2 nanoparticles are grown and packed inside the pores of the AAO membrane, forming well-aligned elongated nanostructures, i.e., nanorods, which have been characterized through electronic microscopy after the removal of the template with KOH (Figure 8). Specifically, the IrO_2 nanorods grew perpendicular to the substrate and present a diameter ranging from 80 to 100 nm, approximately corresponding to the AAO pores dimensions [107]. This IrO_2 nanorods array has been tested as neurotransmitter sensor, displaying a good response to dopamine, chosen as a neurotransmitter model [89].
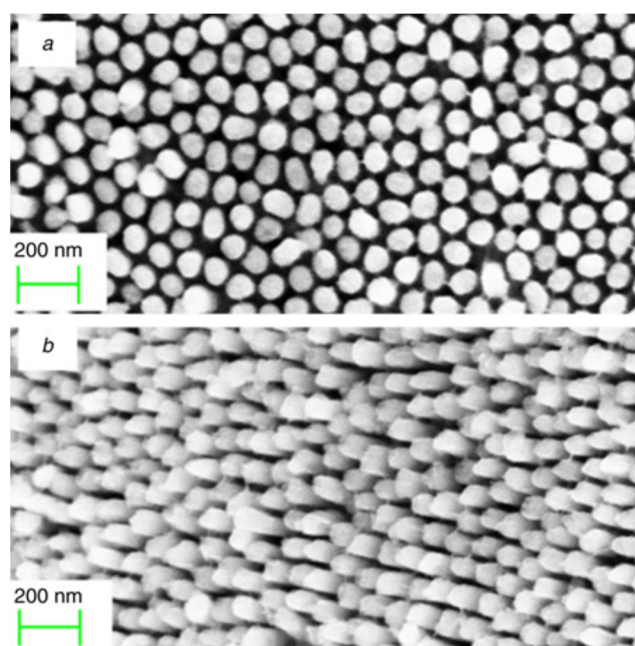
Figure 8. SEM micrographs of IrO_2 nanorods synthetized through the chemical bath route: (**a**) top view; (**b**) tilted view (Reprinted/adapted with permission from Ref. [107]).

IrO_2 nanorods can also be synthesized through the "molten salt" method, a synthetic route similar to the Adams fusions, consisting of the grinding of the Iridium precursor ($IrCl_4$) with NaCl and KCl, followed by the calcinations of the solid mixture at high temperature (600 °C) for 12 h [106]. Through this procedure, Mao et al. obtained nanostructures with an average diameter of 15 nm and length of ca. 200 nm (Figure 9) [106]. However, this method, similarly to the above-described Adams fusion synthesis of IrO_2 nanopowder, required long purification and drying processes. The same authors reported a high electrocatalytic activity of the produced IrO_2 nanorods towards OER, probably attributed to high specific area of the material. Indeed, IrO_2 NRs generate higher OER current density (70 mA/cm^2) than the commercial IrO_2 (58 mA/cm^2) at 0.6 V versus Ag/AgCl electrode in deaerated 0.5 M KOH electrolyte.

Interestingly, within the molten salt method, by carefully varying the $IrCl_4$: NaCl: KCl ratio, it is possible to tune the morphology of the IrO_2 nanostructures [108]. In particular,

it has been reported that, using a $IrCl_4$: NaCl: KCl ratio of 1: 10: 10, nanocubes are obtained (Figure 10a); while changing the $IrCl_4$: NaCl: KCl ratio to 1: 30: 30, a mixture of IrO_2 nanocubes and nanorods is formed (Figure 10b); and ultimately, using a high salts percentage, specifically using a 1: 60: 60 ratio, a sample consisting predominantly of nanorods is obtained (Figure 10c). This experimental observation was explained by Mao et al. considering that the molten salts act both as solvent and as protective layers against aggregation of the formed nanoparticles [108]. Therefore, when the content of salts is low, the growth of nanostructures is allowed in all directions, thus nanocubes can be generated; conversely, when a higher salts percentage is used, the excess of salts block the growth of the nanostructures in all directions, except one, thus nanorods are preferentially formed. Also in this case, the obtained IrO_2 nanorods proved to be excellent electrocatalysts towards OER, displaying high current density, low overpotential, high stability and numerous accessible active sites [108]. The electrocatalytic performance of IrO_2 was again better than commercially available IrO_2.
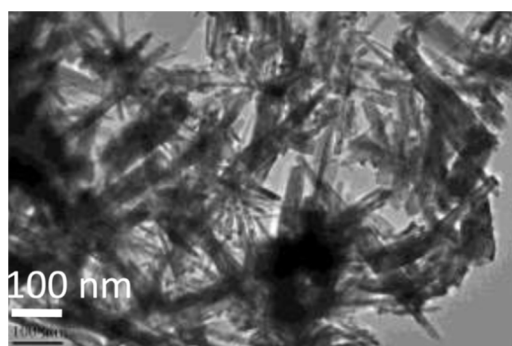
Figure 9. TEM image of IrO_2 nanorods obtained through the molten salt method (Reprinted/adapted with permission from Ref. [106]).
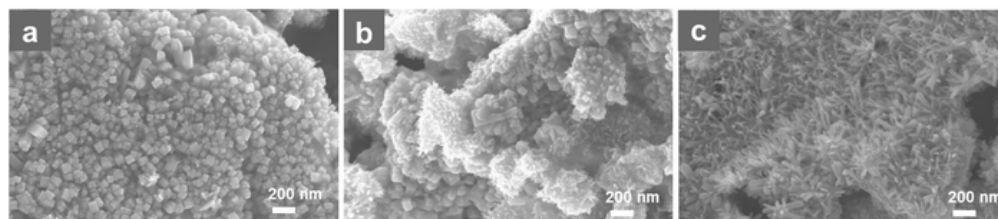
Figure 10. SEM image of the different IrO_2 nanostructures obtained through the molten salt method: (**a**) nanocubes, (**b**) mixture of nanocubes and nanorods, (**c**) nanorods (Reprinted/adapted with permission from Ref. [108]).

IrO_2 nanorods have been also produced through MOCVD technique. In this case, IrO_2 nanorods were grown on Si substrates using a low-melting Iridium source, [(MeCp)Ir(COD)], a high oxygen pressure (10–60 Torr) and a temperature of ca. 350 °C [5,109]. These as-produced IrO_2 nanorods present diameters between 75 and 150 nm, a wedge-shaped morphology and naturally formed sharp tips (Figure 11). However, these nanorods show a polycrystalline nature, characterized by many defects and dislocations.
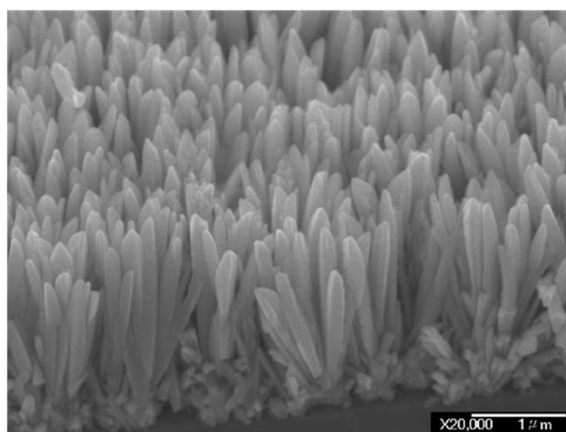
Figure 11. Field-Emission Scanning Electron Microscopy images of the IrO$_2$ nanorods fabricated with this method (Reprinted/adapted with permission from Ref. [5]).

3.3. IrO$_2$ Nanowires/Nanofibres

The MOCVD technique can also be exploited to obtain another type of 1D structures, i.e., IrO$_2$ nanowires, when the experimental parameters are adequately tuned [104,110]. For this purpose, [(MeCp)Ir(COD)] as iridium source, oxygen as both carrier and reactant gas, high temperature (350–400 °C) and high pressure (33 Torr) were needed. By applying these conditions, Zhang et al. synthetized single crystal IrO$_2$ nanowires, having rutile structure, on plasma treated SiO$_2$ substrates covered with a thin metallic layer (Ti, Au, Ni, Co) [110]. The as-obtained nanowires have dimension ranging from 10 to 50 nm in diameter and 1–2 mm in length (Figure 12).
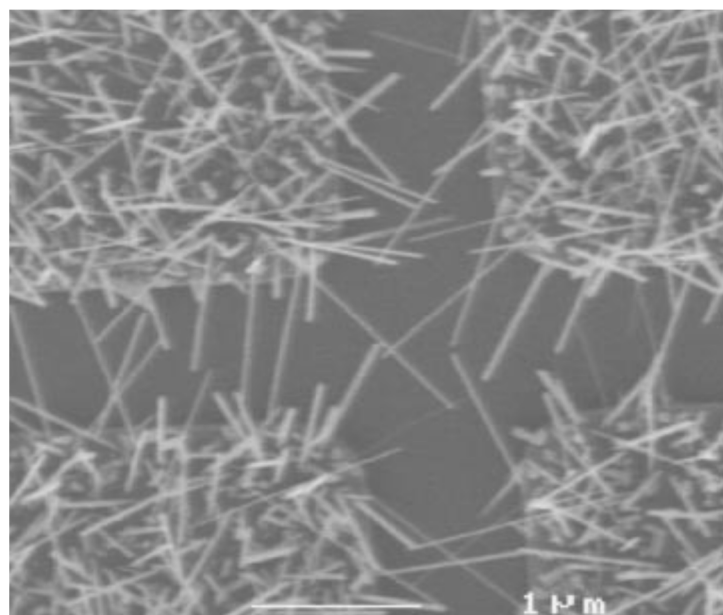
Figure 12. SEM image of IrO$_2$ nanowires obtained through MOCVD (Reprinted/adapted with permission from Ref. [110]).

IrO$_2$ nanowires were also grown on Au microwire and Si/SiO$_2$ substrates via Vapor Phase Transport [48]. IrO$_2$ powder was used as source material and placed in a quartz tube furnace under He and O$_2$ flow. Working at very high temperature (ca. 1000 °C) allows the precursor to sublimate and to be transported by the gas flow to the substrates, where recrystallization occurs in the form of nanowires. Kim et al. reported the preparation of single crystal IrO$_2$ nanowires, displaying lateral dimensions ranging from 20 to 100 nm near

the nanowire tip, with the length extending up to tens of micrometers [48]. Through this method, the formation of nanowires is strongly affected by the O_2 flow. Indeed, without O_2 flow, IrO_2 nanowires are not formed, whereas with a high O_2 flow (50 sccm) polyhedral IrO_2 crystals are generated. IrO_2 nanowires, presenting random orientations have been obtained by using an O_2 flow rate within the range from 10 to 15 sccm. The electrochemical performance of the IrO_2 nanowires grown on the Au microwire was also tested as microelectrode, showing a linear pH response with a super-Nernstian behaviour [48].

IrO_2 nanofibres can be successfully formed through the electrospinning technique [111]. Iridium chloride can be dissolved in ethanol-water together with PVP. The electrospinning of the resulting solution allows the formation of nanofibres of diameter ranging between 50 and 150 nm of diameter (Figure 13a). These as-deposited nanofibres were directly employed for the electrochemical detection of ascorbic acid [112]. More, recently, based on the same synthetic protocol but carrying out a thermal annealing after deposition to ensure the complete removal of the polymer content, amorphous hollow nanofibres of IrO_2 were produced that were of an average diameter of ca. 60 nm (Figure 13b) and were successfully employed for the fabrication of a flexible solid-state gel symmetric supercapacitor [78].
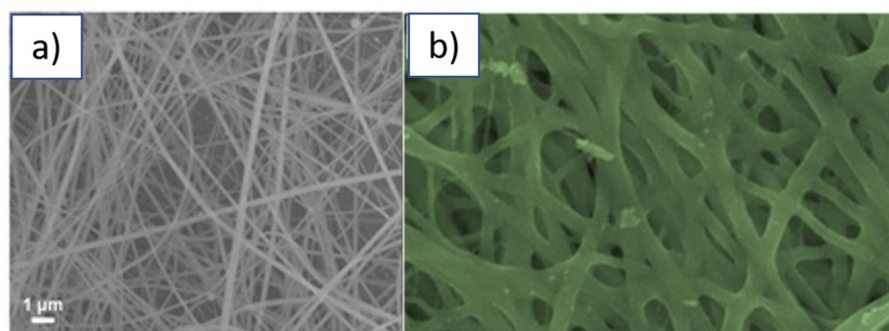
Figure 13. (**a**) nanofibres IrO_2/PVP synthesised through electrospinning (adapted from ref. [111]; (**b**) Hollow nanofibres of IrO_2 after thermal annealing at 300 °C (Reprinted/adapted with permission from Ref. [78]).

4. IrO_2 Nanostructures with Unusual Shapes

The preparation and characterization of IrO_2 nanostructures with unusual shapes have been recently reported. In particular, urchin-like IrO_2 nanostructures have been synthetized through a hydrothermal method, involving the pre-treatment of an aqueous solution of $IrCl_3$ with NaOH and H_2O_2 at 100 °C, followed by heat treatment of the solution at 160–200 °C in autoclave [113]. The urchin-like nanostructures are composed by more levels of structures, specifically short needles, and small cores (Figure 14). By monitoring the hydrothermal synthesis over time, Deng et al. demonstrated that first nanosized IrO_2 spheres with a rough surface are formed upon which thin needles grow in a fractal manner [113]. The urchin-like IrO_2 nanostructures thus obtained have been tested as a catalyst for OER in acidic medium, demonstrating excellent activity and stability in acidic medium, attributable to their hierarchical structure. Indeed, the authors demonstrated that these nanostructures possess improved electrochemical surface-active area with respect to plain spherical IrO_2 structures of a similar size.

Moreover, IrO_2 nanoneedles with an average diameter of 2 nm (Figure 15), have been produced through a modified Adams fusion route, implying the use of 2-mercaptoethylamine (chemical structure reported in Figure 15) in addition to $NaNO_3$ [75]. In this case, the presence of 2-mercaptoethylamine specifically determines the formation of nanoneedles rather than nanopowder. Indeed, without 2-mercaptoethylamine, unshaped and aggregate nanoparticles, like those obtained with the classical Adams fusion method, were obtained. Furthermore, by enhancing the amount of 2-mercaptoethylamine, an increase of the nanoneedles aspect ratio occurs. Also, for IrO_2 nanoneedles, the OER activity has been evaluated, verifying a

better performance with respect to unshaped nanoparticles. However, the exact role of 2-mercaptoethylamine to direct the preferential growth into nanoneedles has not been reported.
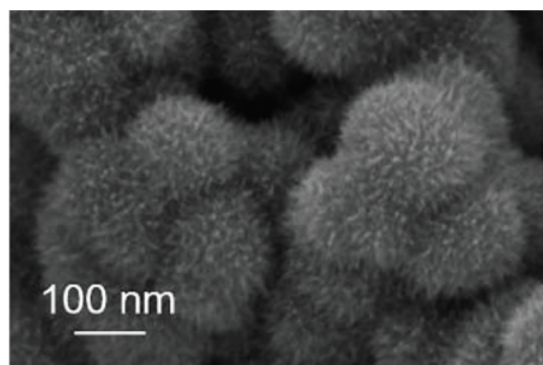
Figure 14. SEM image of urchin-like IrO_2 nanostructures (Reprinted/adapted with permission from Ref. [113]).
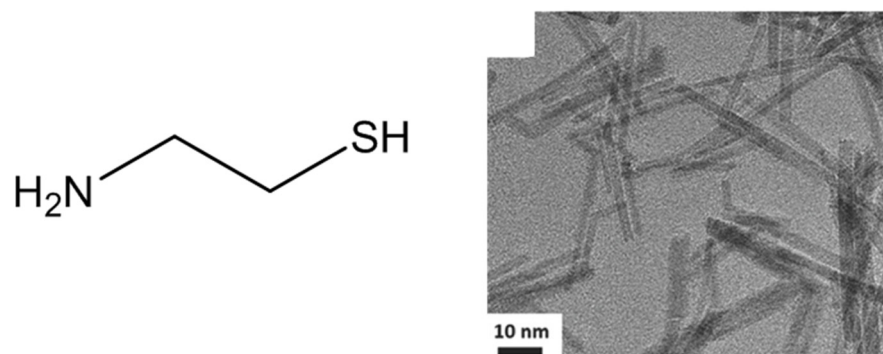
Figure 15. Chemical structure of 2-mercaptoethylamine and TEM image of the IrO_2 nanoneedles (Reprinted/adapted with permission from Ref. [75]).

5. IrO_2 Nanostructured Films

IrO_2 thin films can be prepared through several techniques, ranging from the hard template route [114], to spray pyrolysis [70], to reactive radio-frequency magnetron sputtering [43]. However, the easiest way to introduce a nanostructuration in a metal oxide film, also in an IrO_2 film, is the Evaporation Induced Self-Assembly method (EISA) (Figure 16).
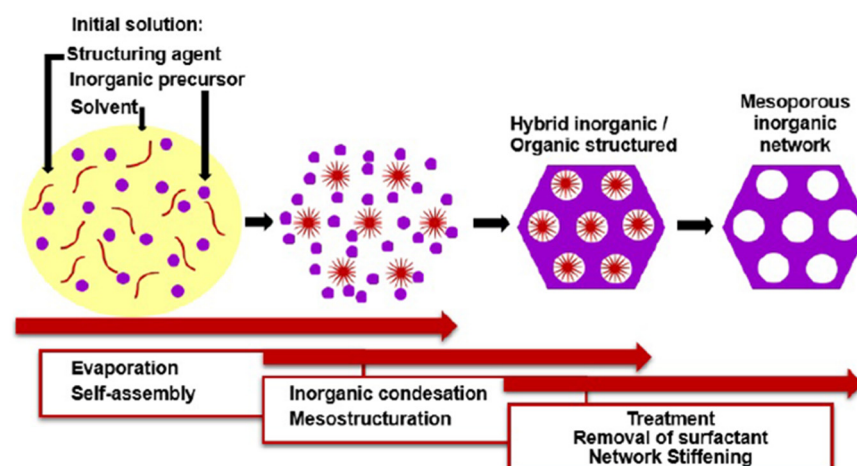
Figure 16. Schematic representation of EISA (Reprinted/adapted with permission from Ref. [115]).

The EISA route involves the use of a soft template, usually an ionic organic surfactant or non-ionic polymeric surfactant which self-assembles into a diversity of supramolecular structures. These latter can be formed of spherical micelles, hexagonal rods, lamellar liquid crystals or other assemblies in solution that self-organise through non-covalent weak interactions such as hydrogen bonding, van der Waals forces, electrostatic interactions and hydrophobic effect. Furthermore, these interactions are also driven by evaporation of the solvent that occurs in situ to the deposition. Hence, these assemblies are the structural directing agents for the formation of inorganic mesostructures. Indeed, the sol–gel precursor hydrolyzes and condenses around the mesostructured self-assembled phase. Subsequent thermal treatment induces the removal of the surfactant, the stiffening of the inorganic network and its crystallization. By varying the type of surfactant, its concentration in the starting solution, and the deposition conditions, it is possible to tune the pore structure and size of the porous materials. EISA is generally coupled with dip-coating or spin-coating deposition techniques, which allow the formation of a thin layer of precursor on different substrates. Through this procedure, Ortel et al. successfully synthesized IrO_2 thin films on different substrates by dip-coating, employing PEO_y-PB_x-PEO_y, (poly(ethylene oxide)-poly(butadiene)-poly(ethylene oxide, chemical structure reported in Figure 17), as templating agent [91,116]. These films presented nanocrystalline mesopores walls and some areas with locally ordered pores (Figure 17). Moreover, their electrocatalytic performance toward OER was tested and compared to untemplated IrO_2 films obtained with the same experimental procedure. The current response on templated IrO_2 films is about 2.1 times higher with respect to the untemplated IrO_2 films, demonstrating the nanostructuration advantages.
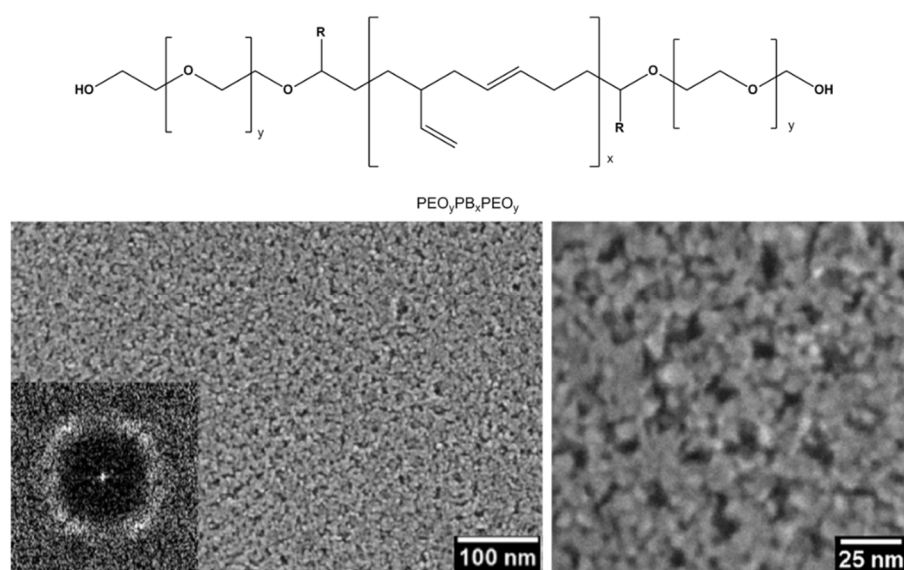
Figure 17. SEM images of IrO_2 mesoporous thin film template with PEO_y-PB_x-PEO_y and calcinated at 500 °C (Reprinted/adapted with permission from Ref. [91]).

Similarly, Chandra et al. developed mesoporous IrO_2 thin films choosing the triblock copolymer "Pluronic F127" ($PEO_{106}PPO_{70}PEO_{106}$, chemical structure reported in Figure 18), as structural directing agent and spin-coating as deposition technique [74,117]. They reported that samples calcinated at 400 °C present 2D hexagonal mesostructure (*p6mm* symmetry, Figure 18), but an increase in treatment temperature entails the transformation into a disordered mesostructure. The enhancement of the electrocatalytic performance toward OER with respect to the untemplated IrO_2 electrode was ca. 2 times higher for mesoporous structure and was ascribed to the larger accessible surface-to-volume ratio.
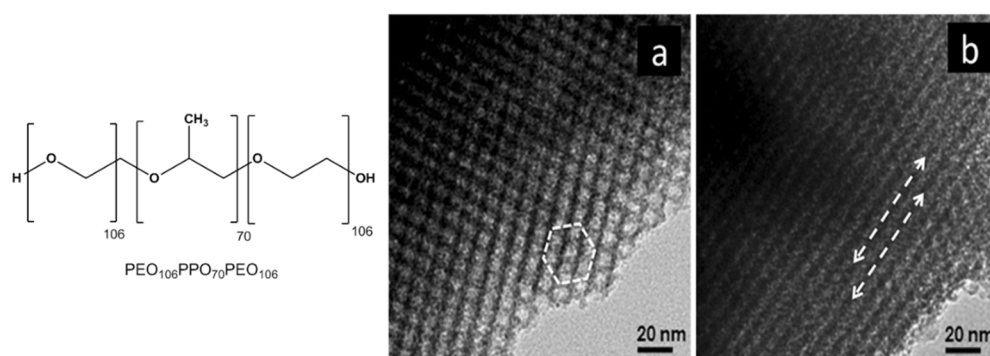
Figure 18. TEM images of mesoporous IrO_2 films template with $PEO_{106}PPO_{70}PEO_{106}$ recorded along the (**a**) [100] and (**b**) [110] axes of the 2D hexagonal structure (Reprinted/adapted with permission from Ref. [74]).

Although EISA appears as a versatile route to induce a nanostructuration into an inorganic material, allowing the modulation of size and shape of the nanostructures and not requiring sophisticated instrumental equipment [118], an important drawback of this technique is its high dependence on experimental parameters. Indeed, temperature, humidity, extraction time and velocity (for dip-coating), concentration of the precursor solution and speed (for spin-coating) would be required as given experimental data for the sake of reproducibility and understanding of the mechanism of nanostructuration. A small amount of variation of these conditions may drastically affect the final nanostructures [119].

The hard-templating route has been also adapted to the preparation of IrO_2 nanostructured films. In this case, colloidal SiO_2 microspheres were immersed in an ethanolic solution of ($H_2IrCl_6 \cdot nH_2O$) to allow the impregnation of the Iridium precursor within the template, then the suspension was dried and calcinated, and the template was removed by using a concentrated HF solution [98]. Chen et al. demonstrated that using SiO_2 microspheres with a mean diameter of 330 nm and very low polydispersity (ca. 0.5%), macroporous IrO_2, displaying an ordered honeycomb array of macropore, can be obtained (Figure 19) [98]. The macropores are typically 300 nm in diameter, which is slightly smaller than the size of SiO_2 microspheres, probably as a consequence of the contraction of the template during the heat treatment process. Although nicely achieved, the main drawback of this synthetical method is the drastic and highly toxic acidic condition (concentrated HF solution) required to remove the templating SiO_2 agent.

Nanostructured IrO_2 films have also been prepared employing an ordered supramolecular gel phase generated by an organometallic Ir(III) complex, used both as templating agent and metal source. Indeed, several Ir(III) complexes can self-assemble in highly organized supramolecular phases in water, including physical gels and lyotropic liquid-crystalline gels [120–122]. Moreover, many metal oxide (SiO_2, TiO_2, ZrO_2, ZnO and WO_3) nanostructures, such as nanotubes, nanoparticles, and nanowires, have been efficiently prepared taking advantage of a supramolecular gel as structural directing agent (SDA) [123]. In this context, the supramolecular gel phase of the Ir(III) compound [(ppy)$_2$Ir(bpy)]EtOCH$_2$CO$_2$ (chemical structure reported in Figure 20), where ppy is 2-phenylpiridine and bpy is 2,2′-bipyridine, which supramolecular architecture in water is built on a double 2D columnar system, was used as template and metal precursor for the preparation of IrO_2 films [122]. The highly ordered metallogel was deposited onto quartz substrates through spin-coating and was left to dry, obtaining the corresponding xerogel, that was calcinated at 600 °C for 4 h, obtaining a uniform IrO_2 thin film. As shown in Figure 19, the film prepared starting from the 5% *w/w* gel phase is composed of ordered vertical IrO_2 arrays that outline its nanostructure, whereas in the case of the 6% *w/w* gel phase, a self-assembled well-ordered multilayer thin film can be observed.
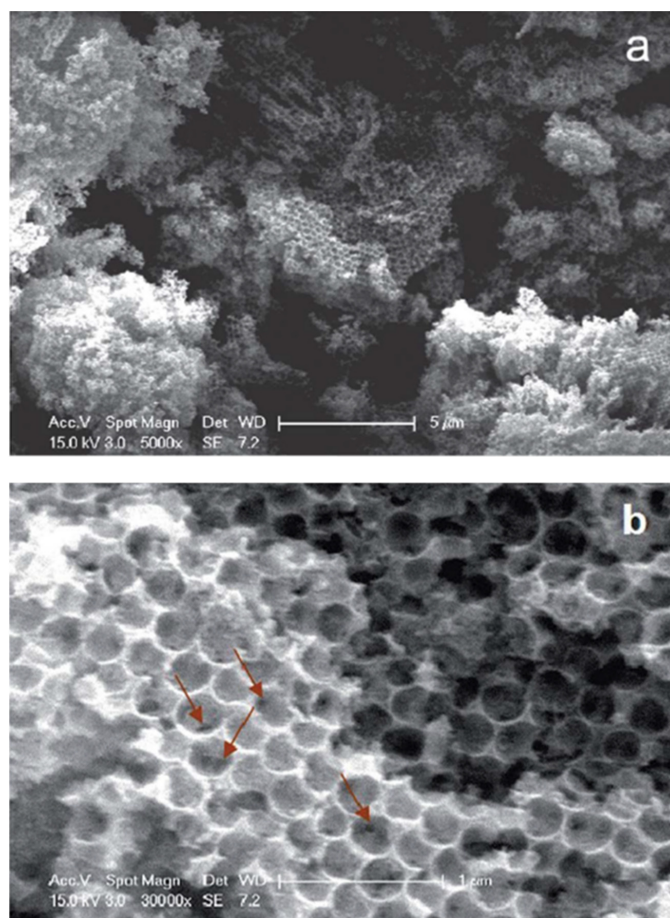
Figure 19. (**a**) Low and (**b**) high magnification SEM images of macroporous IrO_2 prepared by the hard-template method (Reprinted/adapted with permission from Ref. [98]).
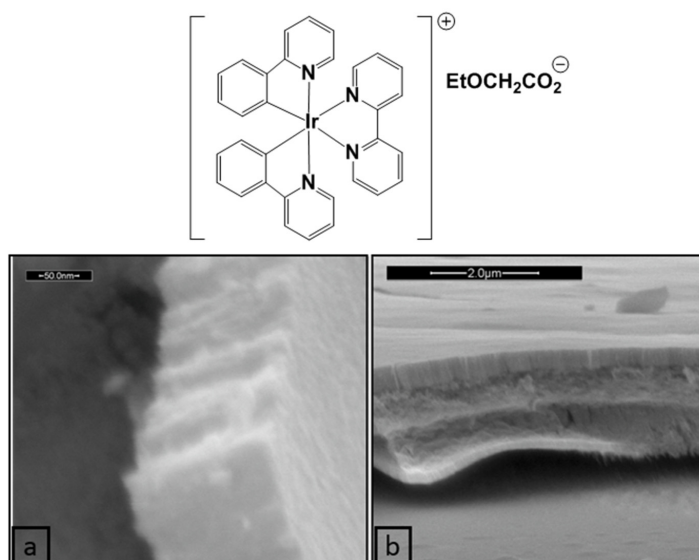
Figure 20. Chemical structure of $[(ppy)_2Ir(bpy)]EtOCH_2CO_2$ and SEM images of the IrO_2 film prepared starting from its 5% *w/w* (**a**) and 6% *w/w* (**b**) gel phase (Reprinted/adapted with permission from Ref. [122]).

Although this study was at its early stage, it clearly shows the possibility of using self-ordered lyotropic Ir(III) complexes for the production of ordered nanostructured thin films of IrO_2, opening a novel alternative route for their preparation.

6. Conclusions

Despite its intrinsic higher cost with respect to other semiconductive metal oxides, IrO_2 does present appealing characteristics that make it the ideal candidate for specific applications. IrO_2 is indeed the only active OER catalyst that is relatively stable in the acidic condition, which is a prerequisite for successful integration with photoanodes to reach optimal photoelectrochemical cells efficiency. As reviewed herein, IrO_2 can be obtained in various types of nanostructured forms allowing the boosting of its performances through mainly the increase of the active surface area owing to the nanoscale architecture. However, to reach such an increment in properties, severe experimental conditions are often required, specific templates or definite substrates must be employed, and a dedicated experimental set-up may also need to be designed. All these factors, of course, will further increase the effective cost of the active nanostructured metal-oxide. Efforts therefore must still be addressed in order to find more sustainable and environmentally friendly access to nanostructured IrO_2-based materials.

Author Contributions: Conceptualization, F.S. and N.G.; writing—original draft preparation, F.S.; reprint permission requests, I.A.; writ-ing—review and editing N.G., A.C. and I.A. All authors have read and agreed to the published version of the manuscript.

Conflicts of Interest: The authors declare no conflict of interest.

References

1. Rogers, D.B.; Shannon, R.D.; Sleight, A.W.; Gillson, J.L. Crystal Chemistry of Metal Dioxides with Rutile-Related Structures. *Inorg. Chem.* **1969**, *8*, 841–849. [CrossRef]
2. Cambridge Crystallographic Data Centre (CCDC), ICSD 640885, deposition number: 1759474. Available online: https://www.ccdc.cam.ac.uk/ (accessed on 2 July 2022).
3. Schultze, J.W.; Trasatti, S. (Eds.) Electrodes of Conductive Metallic Oxides, Part B. Elsevier Scientific Publishing Company, Amsterdam/New York 1981. 702 Seiten, Preis: US $ 83.00/Dfl 170.00. In *Berichte der Bunsengesellschaft für Physikalische Chemie*; John and Wiley and Sons: Hoboken, NJ, USA, 1981; Volume 85, p. 1085. [CrossRef]
4. Riga, J.; Tenret-Noël, C.; Pireaux, J.J.; Caudano, R.; Verbist, J.J.; Gobillon, Y. Electronic Structure of Rutile Oxides TiO_2, RuO_2 and IrO_2 Studied by X-ray Photoelectron Spectroscopy. *Phys. Scr.* **1977**, *16*, 351–354. [CrossRef]
5. Chen, R.S.; Huang, Y.S.; Liang, Y.M.; Tsai, D.S.; Tiong, K.K. Growth and Characterization of Iridium Dioxide Nanorods. *J. Alloys Compd.* **2004**, *383*, 273–276. [CrossRef]
6. Sheng, X.; Li, Z.; Cheng, Y. Electronic and Thermoelectric Properties of V_2O_5, MgV_2O_5, and CaV_2O_5. *Coatings* **2020**, *10*, 453. [CrossRef]
7. Liu, Y.; Masumoto, H.; Goto, T. Preparation of IrO_2 Thin Films by Oxydating Laser-ablated Ir. *Mater. Trans.* **2004**, *45*, 900. [CrossRef]
8. Greiner, M.T.; Lu, Z.-H. Thin-Film Metal Oxides in Organic Semiconductor Devices: Their Electronic Structures, Work Functions and Interfaces. *NPG Asia Mater.* **2013**, *5*, e55. [CrossRef]
9. Xu, B.; Sohn, H.Y.; Mohassab, Y.; Lan, Y. Structures, Preparation and Applications of Titanium Suboxides. *RSC Adv.* **2016**, *6*, 79706–79722. [CrossRef]
10. Yoo, S.-J.; Chang, J.-H.; Lee, J.-H.; Moon, C.-K.; Wu, C.-I.; Kim, J.-J. Formation of Perfect Ohmic Contact at Indium Tin Oxide/N,N′-Di(Naphthalene-1-Yl)-N,N′-Diphenyl-Benzidine Interface Using ReO_3. *Sci. Rep.* **2015**, *4*, 3902. [CrossRef]
11. Pearsall, T.P.; Lee, C.A. Electronic Transport in ReO_3: Dc Conductivity and Hall Effect. *Phys. Rev. B* **1974**, *10*, 2190–2194. [CrossRef]
12. Ben-Dor, L.; Shimony, Y. Crystal Structure, Magnetic Susceptibility and Electrical Conductivity of Pure and NiO-Doped MoO_2 and WO_2. *Mater. Res. Bull.* **1974**, *9*, 837–844. [CrossRef]
13. Lakshminarayana, G.; Kityk, I.V.; Nagao, T. Synthesis, Structural, and Electrical Characterization of RuO_2 Sol–Gel Spin-Coating Nano-Films. *J. Mater. Sci. Mater. Electron.* **2016**, *27*, 10791–10797. [CrossRef]

14. Murakami, Y.; Li, J.; Shimoda, T. Highly Conductive Ruthenium Oxide Thin Films by a Low-Temperature Solution Process and Green Laser Annealing. *Mater. Lett.* **2015**, *152*, 121–124. [CrossRef]

15. Wang, G.; Zheng, J.; Xu, B.; Zhang, C.; Zhu, Y.; Fang, Z.; Yang, Z.; Shang, M.-H.; Yang, W. Tailored Electronic Band Gap and Valance Band Edge of Nickel Oxide via P-Type Incorporation. *J. Phys. Chem. C* **2021**, *125*, 7495–7501. [CrossRef]

16. Jundale, D.M.; Joshi, P.B.; Sen, S.; Patil, V.B. Nanocrystalline CuO Thin Films: Synthesis, Microstructural and Optoelectronic Properties. *J. Mater. Sci. Mater. Electron.* **2012**, *23*, 1492–1499. [CrossRef]

17. Johan, M.R; Suan, M.S.M.; Hawari, N.L.; Ching, H.A. Annealing Effects on the Properties of Copper Oxide Thin Films Prepared by Chemical Deposition. *Int. J. Electrochem. Sci.* **2011**, *6*, 6094–6104.

18. Chang, X.; Wang, T.; Zhang, P.; Zhang, J.; Li, A.; Gong, J. Enhanced Surface Reaction Kinetics and Charge Separation of p–n Heterojunction Co_3O_4/$BiVO_4$ Photoanodes. *J. Am. Chem. Soc.* **2015**, *137*, 8356–8359. [CrossRef]

19. Savio, A.K.P.D.; Fletcher, J.; Smith, K.; Iyer, R.; Bao, J.M.; Robles Hernández, F.C. Environmentally Effective Photocatalyst CoO–TiO_2 Synthesized by Thermal Precipitation of Co in Amorphous TiO_2. *Appl. Catal. B Environ.* **2016**, *182*, 449–455. [CrossRef]

20. Scarpelli, F.; Mastropietro, T.F.; Poerio, T.; Godbert, N. Mesoporous TiO_2 Thin Films: State of the Art. In *Titanium Dioxide—Material for a Sustainable Environment*; InTech: London, UK, 2018.

21. Carcia, P.F.; McCarron, E.M. Synthesis and Properties of Thin Film Polymorphs of Molybdenum Trioxide. *Thin Solid Films* **1987**, *155*, 53–63. [CrossRef]

22. González-Borrero, P.P.; Sato, F.; Medina, A.N.; Baesso, M.L.; Bento, A.C.; Baldissera, G.; Persson, C.; Niklasson, G.A.; Granqvist, C.G.; Ferreira da Silva, A. Optical Band-Gap Determination of Nanostructured WO_3 Film. *Appl. Phys. Lett.* **2010**, *96*, 061909. [CrossRef]

23. Feucht, D.L. Heterojunctions in Photovoltaic Devices. *J. Vac. Sci. Technol.* **1977**, *14*, 57–64. [CrossRef]

24. Batzill, M.; Diebold, U. The Surface and Materials Science of Tin Oxide. *Prog. Surf. Sci.* **2005**, *79*, 47–154. [CrossRef]

25. Pan, C.A.; Ma, T.P. Work Function of In_2O_3 Film as Determined from Internal Photoemission. *Appl. Phys. Lett.* **1980**, *37*, 714–716. [CrossRef]

26. Weiher, R.L.; Ley, R.P. Optical Properties of Indium Oxide. *J. Appl. Phys.* **1966**, *37*, 299–302. [CrossRef]

27. Wei, M.; Li, C.-F.; Deng, X.-R.; Deng, H. Surface Work Function of Transparent Conductive ZnO Films. *Energy Procedia* **2012**, *16*, 76–80. [CrossRef]

28. Srikant, V.; Clarke, D.R. On the Optical Band Gap of Zinc Oxide. *J. Appl. Phys.* **1998**, *83*, 5447–5451. [CrossRef]

29. Sotiropoulou, D.; Ladas, S. The Growth of Ultrathin Films of Copper on Polycrystalline ZrO_2. *Surf. Sci.* **2000**, *452*, 58–66. [CrossRef]

30. Meyer, J.; Zilberberg, K.; Riedl, T.; Kahn, A. Electronic Structure of Vanadium Pentoxide: An Efficient Hole Injector for Organic Electronic Materials. *J. Appl. Phys.* **2011**, *110*, 033710. [CrossRef]

31. Trastoy, J.; Kalcheim, Y.; del Valle, J.; Valmianski, I.; Schuller, I.K. Enhanced Metal–Insulator Transition in V_2O_3 by Thermal Quenching after Growth. *J. Mater. Sci.* **2018**, *53*, 9131–9137. [CrossRef]

32. Li, J. *Oxygen Evolution Reaction in Energy Conversion and Storage: Design Strategies under and Beyond the Energy Scaling Relationship*; Springer Nature Singapore: Singapore, 2022; Volume 14, ISBN 4082002200.

33. Suen, N.T.; Hung, S.F.; Quan, Q.; Zhang, N.; Xu, Y.J.; Chen, H.M. Electrocatalysis for the Oxygen Evolution Reaction: Recent Development and Future Perspectives. *Chem. Soc. Rev.* **2017**, *46*, 337–365. [CrossRef]

34. Ali, I.; AlGhamdi, K.; Al-Wadaani, F.T. Advances in Iridium Nano Catalyst Preparation, Characterization and Applications. *J. Mol. Liq.* **2019**, *280*, 274–284. [CrossRef]

35. Naito, T.; Shinagawa, T.; Nishimoto, T.; Takanabe, K. Recent Advances in Understanding Oxygen Evolution Reaction Mechanisms over Iridium Oxide. *Inorg. Chem. Front.* **2021**, *8*, 2900–2917. [CrossRef]

36. Nabor, G.S.; Hapiot, P.; Neta, P.; Harriman, A. Changes in the Redox State of Iridium Oxide Clusters and Their Relation to Catalytic Water Oxidation. Radiolytic and Electrochemical Studies. *J. Phys. Chem.* **1991**, *95*, 616–621. [CrossRef]

37. Sanchezcasalongue, H.G.; Ng, M.L.; Kaya, S.; Friebel, D.; Ogasawara, H.; Nilsson, A. InSitu Observation of Surface Species on Iridium Oxide Nanoparticles during the Oxygen Evolution Reaction. *Angew. Chem.-Int. Ed.* **2014**, *53*, 7169–7172. [CrossRef] [PubMed]

38. Abe, Y.; Ito, S.; Kim, K.H.; Kawamura, M.; Kiba, T. Electrochromic Properties of Sputtered Iridium Oxide Thin Films with Various Film Thicknesses. *J. Mater. Sci. Res.* **2016**, *6*, 44. [CrossRef]

39. Gottesfeld, S.; McIntyre, J.D.E. Electrochromism in Anodic Iridium Oxide Films: II. PH Effects on Corrosion Stability and the Mechanism of Coloration and Bleaching. *J. Electrochem. Soc.* **1979**, *126*, 742–750. [CrossRef]

40. Gottesfeld, S.; McIntyre, J.D.E.; Beni, G.; Shay, J.L. Electrochromism in Anodic Iridium Oxide Films. *Appl. Phys. Lett.* **1978**, *33*, 208–210. [CrossRef]

41. Dautremont-Smith, W.C. Transition Metal Oxide Electrochromic Materials and Displays: A Review. Part 2: Oxides with Anodic Coloration. *Displays* **1982**, *3*, 67–80. [CrossRef]

42. Shay, J.L.; Beni, G.; Schiavone, L.M. Electrochromism of Anodic Iridium Oxide Films on Transparent Substrates. *Appl. Phys. Lett.* **1978**, *33*, 942–944. [CrossRef]

43. Ito, S.; Abe, Y.; Kawamura, M.; Kim, K.H. Electrochromic Properties of Iridium Oxide Thin Films Prepared by Reactive Sputtering in O_2 or H_2O Atmosphere. *J. Vac. Sci. Technol. B Nanotechnol. Microelectron. Mater. Process. Meas. Phenom.* **2015**, *33*, 041204. [CrossRef]

44. Yamanaka, K. Anodically Electrodeposited Iridium Oxide Films (AEIROF) from Alkaline Solutions for Electrochromic Display Devices. *Jpn. J. Appl. Phys.* **1989**, *28*, 632–637. [CrossRef]
45. Nguyen, C.M.; Huang, W.D.; Rao, S.; Cao, H.; Tata, U.; Chiao, M.; Chiao, J.C. Sol-Gel Iridium Oxide-Based PH Sensor Array on Flexible Polyimide Substrate. *IEEE Sens. J.* **2013**, *13*, 3857–3864. [CrossRef]
46. Ges, I.A.; Ivanov, B.L.; Werdich, A.A.; Baudenbacher, F.J. Differential PH Measurements of Metabolic Cellular Activity in Nl Culture Volumes Using Microfabricated Iridium Oxide Electrodes. *Biosens. Bioelectron.* **2007**, *22*, 1303–1310. [CrossRef] [PubMed]
47. Kuo, L.M.; Chou, Y.C.; Chen, K.N.; Lu, C.C.; Chao, S. A Precise PH Microsensor Using RF-Sputtering IrO_2 and Ta_2O_5 Films on Pt-Electrode. *Sens. Actuators B Chem.* **2014**, *193*, 687–691. [CrossRef]
48. Lee, Y.; Kang, M.; Shim, J.H.; Lee, N.S.; Baik, J.M.; Lee, Y.; Lee, C.; Kim, M.H. Growth of Highly Single Crystalline IrO_2 Nanowires and Their Electrochemical Applications. *J. Phys. Chem. C* **2012**, *116*, 18550–18556. [CrossRef]
49. Hitchman, M.L.; Ramanathan, S. Thermally Grown Iridium Oxide Electrodes for PH Sensing in Aqueous Environments at 0 and 95 °C. *Anal. Chim. Acta* **1992**, *263*, 53–61. [CrossRef]
50. Dobson, J.V.; Snodin, P.R.; Thirsk, H.R. EMF Measurements of Cells Employing Metal—Metal Oxide Electrodes in Aqueous Chloride and Sulphate Electrolytes at Temperatures between 25–250 °C. *Electrochim. Acta* **1976**, *21*, 527–533. [CrossRef]
51. Bordi, S.; Carlá, M.; Papeschi, G.; Pinzauti, S. Iridium/Iridium Oxide Electrode for Potentiometric Determination of Proton Activity in Hydroorganic Solutions at Sub-Zero Temperatures. *Anal. Chem.* **1984**, *56*, 317–319. [CrossRef]
52. O'Hare, D.; Parker, K.H.; Winlove, C.P. Metal-Metal Oxide PH Sensors for Physiological Application. *Med. Eng. Phys.* **2006**, *28*, 982–988. [CrossRef]
53. Bezbaruah, A.N.; Zhang, T.C. Fabrication of Anodically Electrodeposited Iridium Oxide Film PH Microelectrodes for Microenvironmental Studies. *Anal. Chem.* **2002**, *74*, 5726–5733. [CrossRef]
54. Głáb, S.; Hulanicki, A.; Edwall, G.; Folke, F.; Ingman, I.; Koch, W.F. Metal-Metal Oxide and Metal Oxide Electrodes as PH Sensors. *Crit. Rev. Anal. Chem.* **1989**, *21*, 29–47. [CrossRef]
55. Dong, Q.; Sun, X.; He, S. Iridium Oxide Enabled Sensors Applications. *Catalysts* **2021**, *11*, 1164. [CrossRef]
56. Zhang, F.; Ulrich, B.; Reddy, R.K.; Venkatraman, V.L.; Prasad, S.; Vu, T.Q.; Hsu, S.T. Fabrication of Submicron IrO_2 Nanowire Array Biosensor Platform by Conventional Complementary Metal-Oxide-Semiconductor Process. *Jpn. J. Appl. Phys.* **2008**, *47*, 1147–1151. [CrossRef]
57. Quesada-González, D.; Sena-Torralba, A.; Wicaksono, W.P.; de la Escosura-Muñiz, A.; Ivandini, T.A.; Merkoçi, A. Iridium Oxide (IV) Nanoparticle-Based Lateral Flow Immunoassay. *Biosens. Bioelectron.* **2019**, *132*, 132–135. [CrossRef] [PubMed]
58. Zhang, H.; Zhang, L.X.; Zhong, H.; Niu, S.; Ding, C.; Lv, S. Iridium Oxide Nanoparticles-Based Theranostic Probe for in Vivo Tumor Imaging and Synergistic Chem/Photothermal Treatments of Cancer Cells. *Chem. Eng. J.* **2022**, *430*, 132675. [CrossRef]
59. Yuan, X.; Cen, J.; Chen, X.; Jia, Z.; Zhu, X.; Huang, Y.; Yuan, G.; Liu, J. Iridium Oxide Nanoparticles Mediated Enhanced Photodynamic Therapy Combined with Photothermal Therapy in the Treatment of Breast Cancer. *J. Colloid Interface Sci.* **2022**, *605*, 851–862. [CrossRef]
60. Buchanan, R.A.; Lee, I.-S.; Williams, J.M. Surface Modification of Biomaterials through Noble Metal Ion Implantation. *J. Biomed. Mater. Res.* **1990**, *24*, 309–318. [CrossRef]
61. Cogan, S.F.; Ehrlich, J.; Plante, T.D.; Smirnov, A.; Shire, D.B.; Gingerich, M.; Rizzo, J.F. Sputtered Iridium Oxide Films for Neural Stimulation Electrodes. *J. Biomed. Mater. Res. Part B Appl. Biomater.* **2009**, *89B*, 353–361. [CrossRef]
62. Robblee, L.S.; Mangaudis, M.J.; Lasinsky, E.D.; Kimball, A.G.; Brummer, S.B. Charge Injection Properties of Thermally-Prepared Iridium Oxide Films. *MRS Proc.* **1985**, *55*, 303. [CrossRef]
63. Chalamala, B.R.; Wei, Y.; Reuss, R.H.; Aggarwal, S.; Gnade, B.E.; Ramesh, R.; Bernhard, J.M.; Sosa, E.D.; Golden, D.E. Effect of Growth Conditions on Surface Morphology and Photoelectric Work Function Characteristics of Iridium Oxide Thin Films. *Appl. Phys. Lett.* **1999**, *74*, 1394–1396. [CrossRef]
64. Chalamala, B.R.; Wei, Y.; Reuss, R.H.; Aggarwal, S.; Perusse, S.R.; Gnade, B.E.; Ramesh, R. Stability and Chemical Composition of Thermally Grown Iridium-Oxide Thin Films. *J. Vac. Sci. Technol. B Microelectron. Nanom. Struct.* **2000**, *18*, 1919. [CrossRef]
65. Chalamala, B.R.; Reuss, R.H.; Dean, K.A.; Sosa, E.; Golden, D.E. Field Emission Characteristics of Iridium Oxide Tips. *J. Appl. Phys.* **2002**, *91*, 6141–6146. [CrossRef]
66. Kubaschewski, O.; Hopkins, B.E. *Oxidation of Metals and Alloys*, 2nd ed.; Butterworths: London, UK, 1962.
67. Baglio, V.; Sebastián, D.; D'Urso, C.; Stassi, A.; Amin, R.S.; El-Khatib, K.M.; Aricò, A.S. Composite Anode Electrode Based on Iridium Oxide Promoter for Direct Methanol Fuel Cells. *Electrochim. Acta* **2014**, *128*, 304–310. [CrossRef]
68. Chen, Y.M.; Cai, J.H.; Huang, Y.S.; Lee, K.Y.; Tsai, D.S.; Tiong, K.K. A Nanostructured Electrode of IrO x Foil on the Carbon Nanotubes for Supercapacitors. *Nanotechnology* **2011**, *22*, 355708. [CrossRef] [PubMed]
69. Slavcheva, E.; Vitushinsky, R.; Mokwa, W.; Schnakenberg, U. Sputtered Iridium Oxide Films as Charge Injection Material for Functional Electrostimulation. *J. Electrochem. Soc.* **2004**, *151*, E226. [CrossRef]
70. Patil, P.S.; Kawar, R.K.; Sadale, S.B. Electrochromism in Spray Deposited Iridium Oxide Thin Films. *Electrochim. Acta* **2005**, *50*, 2527–2532. [CrossRef]
71. Cui, Z.; Qi, R. First-Principles Simulation of Oxygen Evolution Reaction (OER) Catalytic Performance of IrO_2 Bulk-like Structures: Nanosphere, Nanowire and Nanotube. *Appl. Surf. Sci.* **2021**, *554*, 149591. [CrossRef]
72. Chen, Z.; Duan, X.; Wei, W.; Wang, S.; Ni, B.J. Iridium-Based Nanomaterials for Electrochemical Water Splitting. *Nano Energy* **2020**, *78*, 105270. [CrossRef]

73. González, D.; Sodupe, M.; Rodríguez-Santiago, L.; Solans-Monfort, X. Surface Morphology Controls Water Dissociation on Hydrated IrO$_2$ nanoparticles. *Nanoscale* **2021**, *13*, 14480–14489. [CrossRef]

74. Chandra, D.; Abe, N.; Takama, D.; Saito, K.; Yui, T.; Yagi, M. Open Pore Architecture of an Ordered Mesoporous IrO$_2$ Thin Film for Highly Efficient Electrocatalytic Water Oxidation. *ChemSusChem* **2015**, *8*, 795–799. [CrossRef]

75. Lim, J.; Park, D.; Jeon, S.S.; Roh, C.W.; Choi, J.; Yoon, D.; Park, M.; Jung, H.; Lee, H. Ultrathin IrO$_2$ Nanoneedles for Electrochemical Water Oxidation. *Adv. Funct. Mater.* **2018**, *28*, 1704796. [CrossRef]

76. Nguyen, C.M.; Gurung, I.; Cao, H.; Rao, S.; Chiao, J.C. Fabrication of PH-Sensing Iridium Oxide Nanotubes on Patterned Electrodes Using Anodic Aluminum Oxide Nanotemplate. *Proc. IEEE Sensors* **2013**, *2013*, 1–4. [CrossRef]

77. Khalil, M.; Liu, N.; Lee, R.L. Super-Nernstian Potentiometric PH Sensor Based on the Electrodeposition of Iridium Oxide Nanoparticles. *Int. J. Technol.* **2018**, *9*, 446–454. [CrossRef]

78. Beknalkar, S.A.; Teli, A.M.; Harale, N.S.; Patil, D.S.; Pawar, S.A.; Shin, J.C.; Patil, P.S. Fabrication of High Energy Density Supercapacitor Device Based on Hollow Iridium Oxide Nanofibers by Single Nozzle Electrospinning. *Appl. Surf. Sci.* **2021**, *546*, 149102. [CrossRef]

79. Park, T.J.; Jeong, D.S.; Hwang, C.S.; Park, M.S.; Kang, N.-S. Fabrication of Ultrathin IrO$_2$ Top Electrode for Improving Thermal Stability of Metal–Insulator–Metal Field Emission Cathodes. *Thin Solid Films* **2005**, *471*, 236–242. [CrossRef]

80. Chen, R.-S.; Huang, Y.-S.; Liang, Y.-M.; Hsieh, C.-S.; Tsai, D.-S.; Tiong, K.-K. Field Emission from Vertically Aligned Conductive IrO$_2$ Nanorods. *Appl. Phys. Lett.* **2004**, *84*, 1552–1554. [CrossRef]

81. Gleiter, H. Nanostructured Materials: Basic Concepts and Microstructure. *Acta Mater.* **2000**, *48*, 1–29. [CrossRef]

82. Argon, A.S.; Yip, S. The Strongest Size. *Philos. Mag. Lett.* **2006**, *86*, 713–720. [CrossRef]

83. Huang, C.; Chen, X.; Xue, Z.; Wang, T. Effect of Structure: A New Insight into Nanoparticle Assemblies from Inanimate to Animate. *Sci. Adv.* **2020**, *6*, eaba1321. [CrossRef]

84. Guo, D.; Xie, G.; Luo, J. Mechanical Properties of Nanoparticles: Basics and Applications. *J. Phys. D Appl. Phys.* **2014**, *47*, 013001. [CrossRef]

85. Khan, I.; Saeed, K.; Khan, I. Nanoparticles: Properties, Applications and Toxicities. *Arab. J. Chem.* **2019**, *12*, 908–931. [CrossRef]

86. Rafique, M.; Tahir, M.B.; Rafique, M.S.; Safdar, N.; Tahir, R. *Nanostructure Materials and Their Classification by Dimensionality*; Elsevier: Amsterdam, The Netherlands, 2020; ISBN 9780128211922.

87. Bizzotto, F.; Quinson, J.; Schröder, J.; Zana, A.; Arenz, M. Surfactant-Free Colloidal Strategies for Highly Dispersed and Active Supported IrO$_2$ Catalysts: Synthesis and Performance Evaluation for the Oxygen Evolution Reaction. *J. Catal.* **2021**, *401*, 54–62. [CrossRef]

88. Takimoto, D.; Fukuda, K.; Miyasaka, S.; Ishida, T.; Ayato, Y.; Mochizuki, D.; Shimizu, W.; Sugimoto, W. Synthesis and Oxygen Electrocatalysis of Iridium Oxide Nanosheets. *Electrocatalysis* **2017**, *8*, 144–150. [CrossRef]

89. Nguyen, C.M.; Rao, S.; Chiao, J.C.; Cao, H.; Li, A.; Peng, Y.B. Miniature Neurotransmitter Sensors Featured with Iridium Oxide Nanorods. *Sensors* **2014**, *2014*, 1869–1872. [CrossRef]

90. Tao, Y.; Pan, Z.; Ruch, T.; Zhan, X.; Chen, Y.; Zhang, S.X.; Li, D. Remarkable Suppression of Lattice Thermal Conductivity by Electron-Phonon Scattering in Iridium Dioxide Nanowires. *Mater. Today Phys.* **2021**, *21*, 100517. [CrossRef]

91. Ortel, E.; Reier, T.; Strasser, P.; Kraehnert, R. Mesoporous IrO$_2$ Films Templated by PEO-PB-PEO Block-Copolymers: Self-Assembly, Crystallization Behavior, and Electrocatalytic Performance. *Chem. Mater.* **2011**, *23*, 3201–3209. [CrossRef]

92. Hu, J.; Abdelsalam, M.; Bartlett, P.; Cole, R.; Sugawara, Y.; Baumberg, J.; Mahajan, S.; Denuault, G. Electrodeposition of Highly Ordered Macroporous Iridium Oxide through Self-Assembled Colloidal Templates. *J. Mater. Chem.* **2009**, *19*, 3855–3858. [CrossRef]

93. Quinson, J. Iridium and IrOx Nanoparticles: An Overview and Review of Syntheses and Applications. *Adv. Colloid Interface Sci.* **2022**, *303*, 102643. [CrossRef]

94. Marshall, A.; Børresen, B.; Hagen, G.; Tsypkin, M.; Tunold, R. Preparation and Characterisation of Nanocrystalline IrxSn 1-XO$_2$ Electrocatalytic Powders. *Mater. Chem. Phys.* **2005**, *94*, 226–232. [CrossRef]

95. Bonet, F.; Delmas, V.; Grugeon, S.; Herrera Urbina, R.; Silvert, P.Y.; Tekaia-Elhsissen, K. Synthesis of Monodisperse Au, Pt, Pd, Ru and Ir Nanoparticles in Ethylene Glycol. *Nanostructured Mater.* **1999**, *11*, 1277–1284. [CrossRef]

96. Adams, R.; Shriner, R.L. Platinum oxide as a catalyst in the reduction of organic compounds. iii. preparation and properties of the oxide of platinum obtained by the fusion of chloroplatinic acid with sodium nitrate. *J. Am. Chem. Soc.* **1923**, *45*, 2171–2179. [CrossRef]

97. Cruz, J.C.; Baglio, V.; Siracusano, S.; Ornelas, R.; Ortiz-Frade, L.; Arriaga, L.G.; Antonucci, V.; Aricò, A.S. Nanosized IrO$_2$ Electrocatalysts for Oxygen Evolution Reaction in an SPE Electrolyzer. *J. Nanoparticle Res.* **2011**, *13*, 1639–1646. [CrossRef]

98. Hu, W.; Wang, Y.; Hu, X.; Zhou, Y.; Chen, S. Three-Dimensional Ordered Macroporous IrO$_2$ as Electrocatalyst for Oxygen Evolution Reaction in Acidic Medium. *J. Mater. Chem.* **2012**, *22*, 6010–6016. [CrossRef]

99. Zhang, J.; Liu, S.; Wang, H.; Xia, Q.; Huang, X. Polypyrrole Assisted Synthesis of Nanosized Iridium Oxide for Oxygen Evolution Reaction in Acidic Medium. *Int. J. Hydrog. Energy* **2020**, *45*, 33491–33499. [CrossRef]

100. Diaz, C.; Valenzuela, M.L.; Cifuentes-Vaca, O.; Segovia, M.; Laguna-Bercero, M.A. Iridium Nanostructured Metal Oxide, Its Inclusion in Silica Matrix and Their Activity toward Photodegradation of Methylene Blue. *Mater. Chem. Phys.* **2020**, *252*, 123276. [CrossRef]

101. Chen, P.C.; Chen, Y.C.; Huang, C.N. Free-Standing Iridium Oxide Nanotube Array for Neural Interface Electrode Applications. *Mater. Lett.* **2018**, *221*, 293–295. [CrossRef]

102. Yu, A.; Kwon, T.; Lee, C.; Lee, Y. Highly Catalytic Electrochemical Oxidation of Carbon Monoxide on Iridium Nanotubes: Amperometric Sensing of Carbon Monoxide. *Nanomaterials* **2020**, *10*, 1140. [CrossRef]
103. Chen, R.S.; Huang, Y.S.; Tsai, D.S.; Chattopadhyay, S.; Wu, C.T.; Lan, Z.H.; Chen, K.H. Growth of Well Aligned IrO$_2$ Nanotubes on LiTaO$_3$(012) Substrate. *Chem. Mater.* **2004**, *16*, 2457–2462. [CrossRef]
104. Chen, R.S.; Korotcov, A.; Huang, Y.S.; Tsai, D.S. One-Dimensional Conductive IrO$_2$ nanocrystals. *Nanotechnology* **2006**, *17*, R67–R87. [CrossRef]
105. Shan, C.C.; Tsai, D.S.; Huang, Y.S.; Jian, S.H.; Cheng, C.L. Pt-Ir-IrO$_2$NT Thin-Wall Electrocatalysts Derived from IrO$_2$ Nanotubes and Their Catalytic Activities in Methanol Oxidation. *Chem. Mater.* **2007**, *19*, 424–431. [CrossRef]
106. Ahmed, J.; Mao, Y. Ultrafine Iridium Oxide Nanorods Synthesized by Molten Salt Method toward Electrocatalytic Oxygen and Hydrogen Evolution Reactions. *Electrochim. Acta* **2016**, *212*, 686–693. [CrossRef]
107. Nguyen, C.M.; Thumthan, O.; Huang, C.; Tata, U.; Hao, Y.; Chiao, J.C. Chemical Bath Method to Grow Precipitated Nanorods of Iridium Oxide on Alumina Membranes. *Micro Nano Lett.* **2012**, *7*, 1256–1259. [CrossRef]
108. Mohan, S.; Gupta, S.K.; Mao, Y. Morphology-Oxygen Evolution Activity Relationship of Iridium(Iv) Oxide Nanomaterials. *New J. Chem.* **2022**, *46*, 3716–3726. [CrossRef]
109. Chen, R.S.; Huang, Y.S.; Liang, Y.M.; Tsai, D.S.; Chi, Y.; Kai, J.J. Growth Control and Characterization of Vertically Aligned IrO$_2$ Nanorods. *J. Mater. Chem.* **2003**, *13*, 2525–2529. [CrossRef]
110. Zhang, F.; Barrowcliff, R.; Stecker, G.; Pan, W.; Wang, D.; Hsu, S.T. Synthesis of Metallic Iridium Oxide Nanowires via Metal Organic Chemical Vapor Deposition. *Jpn. J. Appl. Phys. Part 2 Lett.* **2005**, *44*, L398–L401. [CrossRef]
111. Lee, J.; Yang, H.-S.; Lee, N.-S.; Kwon, O.; Shin, H.-Y.; Yoon, S.; Baik, J.M.; Seo, Y.-S.; Kim, M.H. Hierarchically Assembled 1-Dimensional Hetero-Nanostructures: Single Crystalline RuO$_2$ Nanowires on Electrospun IrO$_2$ Nanofibres. *CrystEngComm* **2013**, *15*, 2367. [CrossRef]
112. Kim, S.; Kim, Y.L.; Yu, A.; Lee, J.; Lee, S.C.; Lee, C.; Kim, M.H.; Lee, Y. Electrospun Iridium Oxide Nanofibers for Direct Selective Electrochemical Detection of Ascorbic Acid. *Sens. Actuators B Chem.* **2014**, *196*, 480–488. [CrossRef]
113. Deng, Q.; Sun, Y.; Wang, J.; Chang, S.; Ji, M.; Qu, Y.; Zhang, K.; Li, B. Boosting OER Performance of IrO$_2$ in Acid via Urchin-like Hierarchical-Structure Design. *Dalt. Trans.* **2021**, *50*, 6083–6087. [CrossRef]
114. Comstock, D.J.; Christensen, S.T.; Elam, J.W.; Pellin, M.J.; Hersam, M.C. Synthesis of Nanoporous Activated Iridium Oxide Films by Anodized Aluminum Oxide Templated Atomic Layer Deposition. *Electrochem. Commun.* **2010**, *12*, 1543–1546. [CrossRef]
115. Machado, A.E.H.; Borges, K.A.; Silva, T.A.; Santos, L.M.; Borges, M.F.; Machado, W.A.; Caixeta, B.P.; Oliveira, S.M.; Trovó, A.G.; Patrocínio, A.O.T. Applications of Mesoporous Ordered Semiconductor Materials—Case Study of TiO$_2$. In *Solar Radiation Applications*; InTech: Rijeka, Croatia, 2015.TiO2. In *Solar Radiation Applications*; InTech: Rijeka, Croatia, 2015.
116. Bernicke, M.; Ortel, E.; Reier, T.; Bergmann, A.; Ferreira de Araujo, J.; Strasser, P.; Kraehnert, R. Iridium Oxide Coatings with Templated Porosity as Highly Active Oxygen Evolution Catalysts: Structure-Activity Relationships. *ChemSusChem* **2015**, *8*, 1908–1915. [CrossRef]
117. Chandra, D.; Sato, T.; Tanahashi, Y.; Takeuchi, R.; Yagi, M. Facile Fabrication and Nanostructure Control of Mesoporous Iridium Oxide Films for Efficient Electrocatalytic Water Oxidation. *Energy* **2019**, *173*, 278–289. [CrossRef]
118. Brinker, C.J.; Lu, Y.; Sellinger, A.; Fan, H. ChemInform Abstract: Evaporation-Induced Self-Assembly: Nanostructures Made Easy. *Adv. Mater.* **1999**, *11*, 579. [CrossRef]
119. Grosso, D.; Cagnol, F.; Soler-Illia, G.; Crepaldi, E.L.; Amenitsch, H.; Brunet-Bruneau, A.; Bourgeois, A.; Sanchez, C. Fundamentals of Mesostructuring through Evaporation-Induced Self-Assembly. *Adv. Funct. Mater.* **2004**, *14*, 309–322. [CrossRef]
120. Scarpelli, F.; Ricciardi, L.; La Deda, M.; Brunelli, E.; Crispini, A.; Ghedini, M.; Godbert, N.; Aiello, I. A Luminescent Lyotropic Liquid-Crystalline Gel of a Water-Soluble Ir(III) Complex. *J. Mol. Liq.* **2021**, *334*, 116187. [CrossRef]
121. Scarpelli, F.; Ionescu, A.; Ricciardi, L.; Plastina, P.; Aiello, I.; La Deda, M.; Crispini, A.; Ghedini, M.; Godbert, N. A Novel Route towards Water-Soluble Luminescent Iridium(III) Complexes: Via a Hydroxy-Bridged Dinuclear Precursor. *Dalt. Trans.* **2016**, *45*, 17264–17273. [CrossRef]
122. Scarpelli, F.; Ionescu, A.; Aiello, I.; La Deda, M.; Crispini, A.; Ghedini, M.; Brunelli, E.; Sesti, S.; Godbert, N. High Order in a Self-Assembled Iridium(III) Complex Gelator Towards Nanostructured IrO$_2$ Thin Films. *Chem.-Asian J.* **2017**, *12*, 2703–2710. [CrossRef] [PubMed]
123. Llusar, M.; Sanchez, C. Inorganic and Hybrid Nanofibrous Materials Templated with Organogelators. *Chem. Mater.* **2008**, *20*, 782–820. [CrossRef]